ACS APPLIED BIO MATERIALS

www.acsabm.org Article

Nanostructured Polymer Monoliths for Biomedical Delivery Applications

Yihui Xie and Marc A. Hillmyer*

Cite This: *ACS Appl. Bio Mater.* 2020, 3, 3236−3247 Read Online

ACCESS | Metrics & More | Article Recommendations | Supporting Information

ABSTRACT: Drug delivery systems are designed to control the release rate and location of therapeutic agents in the body to achieve enhanced drug efficacy and to mitigate adverse side effects. In particular, drug-releasing implants provide sustained and localized release. We report nanostructured polymer monoliths synthesized by polymerization-induced microphase separation (PIMS) as potential implantable delivery devices. As a model system, free poly(ethylene oxide) homopolymers were incorporated into the nanoscopic poly(ethylene oxide) domains contained within a cross-linked polystyrene matrix. The *in vitro* release of these poly(ethylene oxide) molecules from monoliths was investigated as a function of poly(ethylene oxide) loading and molar mass as well as the molar mass and weight fraction of poly(ethylene oxide) macro-chain transfer agent used in the PIMS process for forming the monoliths. We also developed nanostructured microneedles targeting efficient and long-term transdermal drug delivery by combining PIMS and microfabrication techniques. Finally, given the prominence of poly(lactide) in drug delivery devices, the degradation rate of microphase-separated poly(lactide) in PIMS monoliths was evaluated and compared with bulk poly(lactide).

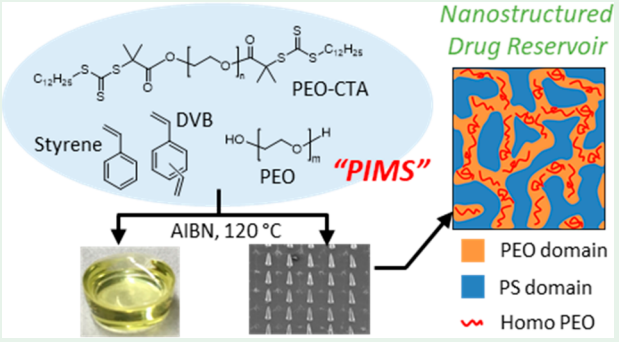

KEYWORDS: *nanostructured polymers, self-assembly, medical implants, drug delivery, release kinetics, microneedles*

INTRODUCTION

Controlled drug delivery systems are designed to enhance the effectiveness of drug therapy by controlling the release rate of therapeutic agents and the location where they are released in the body.[1] The improved control over temporal and spatial distribution of a drug allows better drug efficacy and specificity with a lower incidence of adverse side effects.[2,3] Controlled release systems may also protect a drug from degradation and premature elimination, help the drug cross physiological barriers, and increase patient compliance by reducing the frequency of administration.[4−6] Remarkable progress has been made in nanoscale systems for drug delivery, fueled by innovations in material chemistry and nanotechnology.[7] On-demand release using stimuli-responsive materials as well as efficient targeting through ligation has been realized by numerous sophisticated nanocarriers.[7−9] Apart from the advanced nanoparticulate materials for oral or intravenous administration,[10−12] implantable drug-releasing systems have recently received tremendous attention.[13] Drug-releasing implants provide sustained and localized release. Polymer-based implants have been intensively explored for clinical applications, such as cancer therapy, gene delivery, birth control, bone and tissue regeneration, and as therapeutic contact lenses.[13,14] In a recent example, Padmakumar et al. fabricated a woven polydioxanone nanotextile through electrospinning, which could be loaded with paclitaxel (PTX). *In vitro* and *in vivo* drug release tests demonstrated long-term and tunable PTX release, which was achieved by adjusting the packing density of the polymeric nanotextile implants.[15] Beyond traditional implants, microneedles have drawn attention for painless transdermal drug delivery to improve patient compliance.[16] Microneedles are micrometer-sized needles that can pierce the skin in a painless manner and facilitate the transdermal drug delivery. Unlike traditional hypodermic needles, microneedles are minimally invasive without stimulating pain receptors in the dermis due to their small size but long enough to bypass the stratum corneum (SC) barrier, the outmost 15−20 μm layer of skin formed by dead corneocytes.[17−21]

In most monolithic devices, drugs are loaded directly into homogeneous polymer matrices, such as widely used hydrogel delivery systems. In a recent review, Li et al. concluded that the mesh size (solvent-rich spaces between swollen and cross-

Received: February 28, 2020
Accepted: April 7, 2020
Published: April 21, 2020

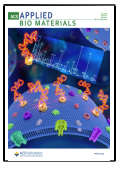

https://dx.doi.org/10.1021/acsabm.0c00228
ACS Appl. Bio Mater. 2020, 3, 3236−3247

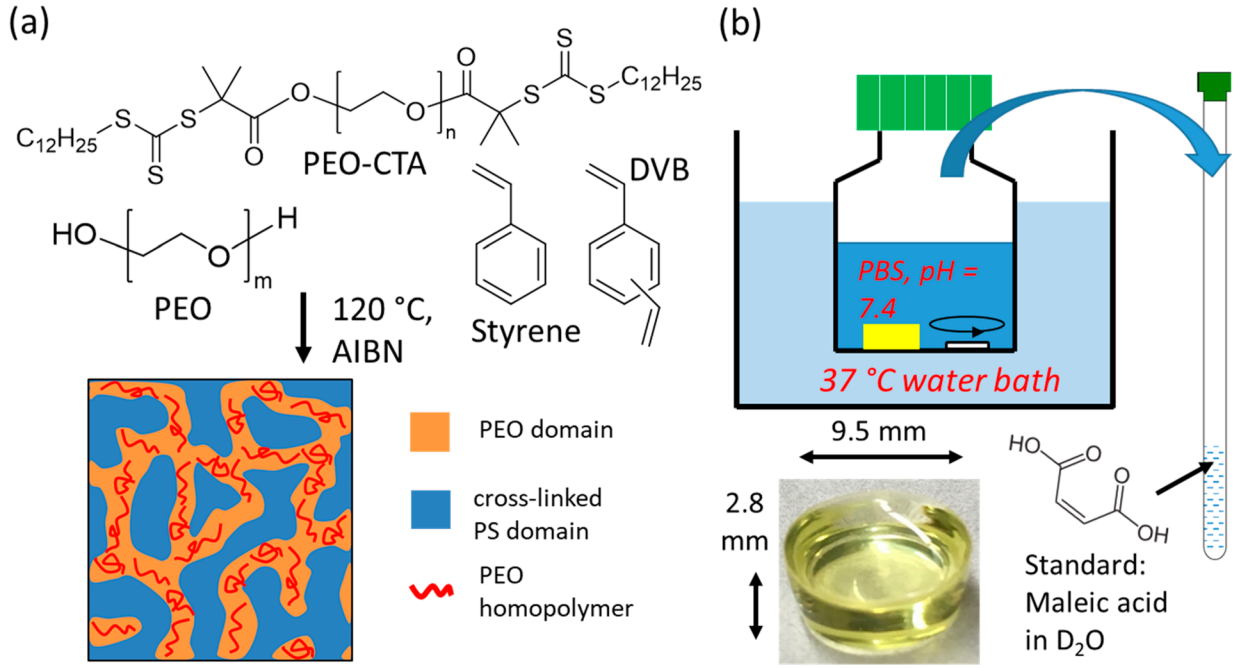

Figure 1. (a) Preparation of PEO-loaded polymer monoliths. After a mixture of PEO-CTA, PEO homopolymer (hPEO), and styrene/DVB (s/DVB) was heated at 120 °C in the presence of 2,2′-azobis(2-methylpropionitrile) (AIBN), a cross-linked PEO-*b*-P(S-*co*-DVB) monolith is formed with the PEO domain microphase separated from the P(S-*co*-DVB) matrix. (b) hPEO release experiments where a cylinder-shaped hPEO-loaded monolith tablet (9.5 mm diameter × 2.8 mm height) is immersed in PBS (pH = 7.4) at 37 °C. Aliquots are taken at different times and mixed with D_2O containing maleic acid as an internal standard to determine the amount of hPEO released using ^1H NMR spectroscopy.

linked polymer chains) prominently determines how drugs diffuse inside the cross-linked network of hydrogel delivery systems with steric interactions, and experimentally, the mesh size in homopolymer hydrogels is governed by polymer entanglements and cross-linker concentration.[22] Here, we add one more dimension to control drug release, reporting nanostructured block polymer monoliths with interpenetrating bicontinuous "drug-philic" (reminiscent of poly(ethylene glycol) (PEG) hydrogels) and "drug-phobic" domains as potential drug-releasing implants. Nanostructures have emerged recently for targeted and efficient drug delivery.[23−25] Yet, very few monolithic delivery systems with well-defined continuous nanostructures at the 10 nm scale have been reported. Our group has developed nanostructured polymer monoliths through polymerization-induced microphase separation (PIMS).[26] This process is a form of bulk reversible addition−fragmentation chain-transfer (RAFT) polymerization used to prepare microstructured block polymer thermosets with features on the order of tens of nanometers. A chemically degradable polymer functionalized with a RAFT chain-transfer agent (macro-CTA) such as poly(ethylene oxide) (PEO) or poly(lactide) (PLA) is used to form diblocks with a high T_g polymer that provides structural rigidity, such as poly(styrene-*co*-divinylbenzene) P(S-*co*-DVB). The macro-CTA is dissolved in a mixture of mono- and difunctional monomers. Chain extension to form a diblock polymer occurs from the functional end of macro-CTA. Due to the incompatibility of the two segments, microphase separation takes place, and the diblock gradually evolves into a transient disordered bicontinuous network morphology. Before it forms thermodynamically stable morphologies dictated by the volume fraction of each segment, this bicontinuous nanostructure is kinetically captured by simultaneous cross-linking with the difunctional monomer. The resulting cross-linked monoliths can be transformed to mesoporous materials by selectively removing the etchable PLA domain through basic hydrolysis.[27] Related nanoporous polymers have also been prepared using a different block polymer microphase separation approach.[28] PIMS is more efficient for obtaining an isotropic percolating nanopore structure in a robust polymer monolith without an additional annealing or aligning step. Use of a functional rather than a sacrificial macro-CTA has been previously demonstrated by preparation of conductive PIMS polymer electrolyte membranes incorporating ionic liquids into the interpenetrating PEO domain.[29−31] Additionally, fast decoloration of photochromic dye has been achieved by attaching the dye covalently into the liquid-like P4MCL domain in a rigid PMMA matrix.[32]

In the nanostructured polymer monolith prepared in this study, the cross-linked polystyrene (PS) domain maintains the predefined geometry of the monolith during release, while the hydrophilic PEO domain stores the drug and mediates its diffusion. The nanostructure of the domain through which the drug diffuses is expected to offer additional control over the release behavior, because the size and number of diffusion channels can be tuned by various fabrication parameters. Meanwhile, it is interesting to study how a cocontinuous structure in a confined environment would affect drug release. The *in vitro* release of model PEO homopolymers (hPEO) from monoliths was investigated as a function of hPEO loading and molar mass as well as the molar mass and weight fraction of the PEO macro-CTA used for the preparation of the monoliths. We propose these monoliths could be subcutaneously administrated by surgery for long-term drug delivery, given the robustness of the polymer matrix. There are already successful commercial examples of solid implantable drug-releasing monoliths in the market (e.g., Supprelin, Jadelle, Implanon, and Osurdex), which are good models for future *in vivo* release experiments. Moreover, this in situ cross-linking

https://dx.doi.org/10.1021/acsabm.0c00228
ACS Appl. Bio Mater. 2020, 3, 3236−3247

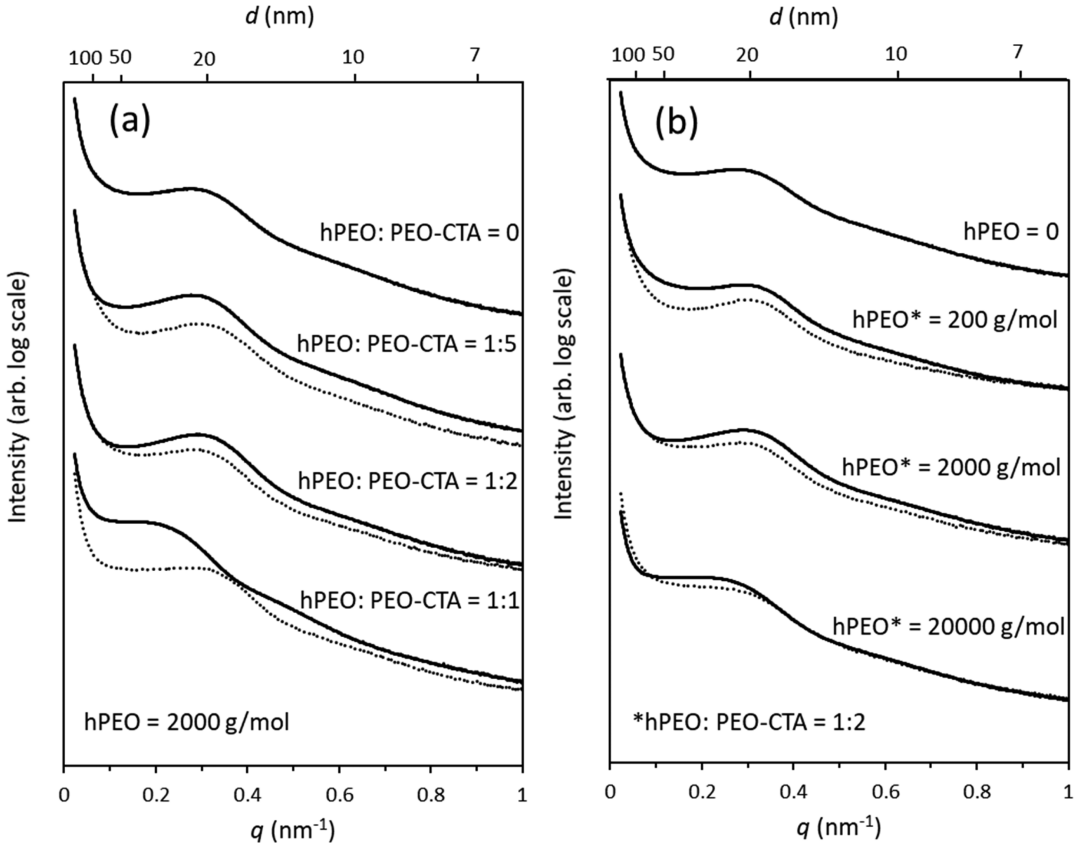

Figure 2. (a) Small-angle X-ray scattering of PEO-*b*-P(S-*co*-DVB) monoliths prepared with (a) different hPEO loadings (solid line, domain spacing, d = 20, 20, 19, and 25 nm from top to bottom) and same molar masses (2000 g mol^{-1}). Dotted lines indicate the samples after hPEO release (d = 18, 19, and 18 nm from top to bottom). (b) Different hPEO molar masses (solid line, d = 20, 19, 19, and 22 nm from top to bottom) and same loadings (hPEO:PEO-CTA = 1:2). PEO-CTA (20 kg/mol) (PEO-CTA:S/DVB = 8:17) was used in all the samples. Dotted lines indicate the samples after hPEO release (d = 19, 19, and 21 nm from top to bottom).

and nanostructure formation process imparts outstanding ability to tailor the macroscopic shape of the monoliths for particular applications. We demonstrated this feature by successfully fabricating conical microneedles with the same nanostructure as cylindrical monoliths. Our prototypes are the first microneedles based on nanostructured block polymers ever reported. Finally, besides their transport behavior, the biodegradability is another crucial property for drug delivery biomaterials. As a prevalent polymer for biomedical implants, PLA's degradation rate has been intensively studied and engineered with physicochemical approaches.[33] We disclose an interesting nanostructure-accelerated degradation of PLA in PIMS monoliths, which could serve as a new regulating mechanism for degradation-induced release.[34]

RESULTS AND DISCUSSION

Experimental Design. Nanostructured monoliths were fabricated by in situ polymerization of styrene and divinylbenzene (DVB) in the presence of PEO-macro-chain transfer agent (PEO-CTA) as shown in Figure 1a. The reversible addition−fragmentation chain-transfer (RAFT) mechanism enables the growth of PS from the termini of PEO-CTA. The chemical incompatibility between the growing PS and PEO drives the microphase separation of the two segments, while DVB cross-linking kinetically arrests the bicontinuous disordered morphology. Thus, the hydrophilic domains are comprised of PEO embedded in a cross-linked P(S-*co*-DVB) matrix and can, in principle, be loaded with hydrophilic drugs during the PIMS process. Upon implantation and exposure to aqueous environments, such active ingredients could diffuse through the PEO domains of the monolith. Although a PS homopolymer is not commonly used for medical implants, a PS-based triblock copolymer, polystyrene-*b*-polyisobutylene-*b*-polystyrene (SIBS), has been coated on vascular stents for drug release in the blood vessel.[35] SIBS also shows excellent biocompatibility as an FDA-approved biomaterial.[36]

Hydroxytelechelic PEO homopolymers (hPEOs) were chosen as model compounds to study the release, because (1) we expect hPEO to be readily incorporated into PEO domains in the block polymer monoliths; (2) the wide range of available molar masses of PEO allows us to explore the impact of hPEO length; (3) many drugs are conjugated to PEO to improve the stability and solubility in the human body, and thus, hPEO is a model for such drug conjugates.[37] In a typical monolith synthesis, the polymerization mixture consisting of PEO-CTA, hPEO, and S/DVB ([S]:[DVB] = 4:1) was heated at 120 °C for 24 h in the presence of azobis(isobutyronitrile) (AIBN) as a thermal radical initiator (see Supporting Information for synthesis details). Four parameters, (1) the mass ratio of hPEO to PEO-CTA (hPEO:PEO-CTA), (2) the molar masses of hPEO, (3) the molar mass of PEO-CTA, and (4) the mass ratio of PEO-CTA to S/DVB monomers in the base PIMS polymerization mixture, were varied. The morphologies of monoliths at different stages, prerelease, postrelease, and after degradative chemical etching of all PEO

https://dx.doi.org/10.1021/acsabm.0c00228
ACS Appl. Bio Mater. 2020, 3, 3236−3247

species with hydroiodic acid (HI), were characterized by scanning electron microscopy (SEM), small-angle X-ray scattering (SAXS), and N_2 sorption experiments.

To quantitatively study the release kinetics of hPEO, we prepared monoliths from the prepolymer solution of a fixed total weight (200 mg) in glass vials of the same size throughout the entire study to maintain a consistent size and shape of monoliths. The average mass of the undamaged cylinder-shaped monolith tablets was 180 ± 8 mg with an average diameter of about 9.5 mm and thickness of about 2.8 mm. Figure 1(b) shows the release experiment where a monolith was submerged in 5 mL of a 37 °C, pH 7.4 phosphate-buffered saline (PBS) solution (see Supporting Information for experiment details). To determine the amount of hPEO released to the solution after certain time, an aliquot was taken from it and mixed with D_2O containing a known mass of maleic acid as an internal standard. The hPEO content was calculated based on the relative integral values of the characteristic peak of PEO to maleic acid as shown in Figure S2. The error of the quantitative NMR measurement was estimated to be about ±0.68 mg/mL (±3%) when tested with an aqueous solution containing 23 mg/mL of 2 kg mol^{-1} hPEO. The total loading of hPEO in the monolith was assumed to be equal to the initial amount of hPEO that was precisely weighed and added to the polymerization mixture during the monolith preparation.

Morphological Study. In Figure 2a, a monolith prepared using 20 kg mol^{-1} PEO-CTA (PEO-CTA:S/DVB = 8:17) and no hPEO (hPEO:PEO-CTA = 0) shows a single broad SAXS reflection centered at a scattering wavevector $q \approx 0.3$ nm^{-1}, indicating a microphase-separated but disordered structure with compositional heterogeneity on an ~20 nm length scale. This result is similar to the nanostructured monoliths that our previous studies achieved, although here a difunctional instead of monofunctional PEO-CTA was employed.[29−31] We have reported that PEO[38] or PLA[39] homopolymer selectively swells the microphase-separated PLA domain in PLA-*b*-P(S-*co*-DVB) monoliths. When the homopolymer additive exceeds the solubility limit in the PLA domain by increasing either the molar mass or mass fraction of the additive, macrophase separation of the homopolymer occurs, resulting in macropores.

In this work, macrophase separation of hPEO was absent in all the hPEO-containing samples, because the content of hPEOs is below their solubility limit in the PEO domain. N_2 sorption isotherms indicate there is no significant sorption (i.e., no significant porosity) from the postrelease sample, suggesting all the hPEO was distributed homogeneously in the PEO domain, and no voids were formed by the removal of hPEO (Figure S3). After etching with HI, N_2 sorption shows type IV isotherms with H2 hysteresis, which are consistent with an interconnected mesoporous structure with features at the 10 nm scale (see Figures S3 and S4). In Figure 3a, the SEM image of a representative monolith after hPEO release shows the rough surface of a fractured sample without any evidence of macropores. The interconnected mesoporous structure induced by microphase separation can be imaged by SEM after PEO domain was removed as shown in Figure 3b for one of the samples, which supports the SAXS and N_2 sorption measurements.

Effect of hPEO Loading. Our hPEO blending experiments were carried out by the addition of hPEO to a base PIMS mixture containing a fixed mass ratio (PEO-CTA:S/DVB =

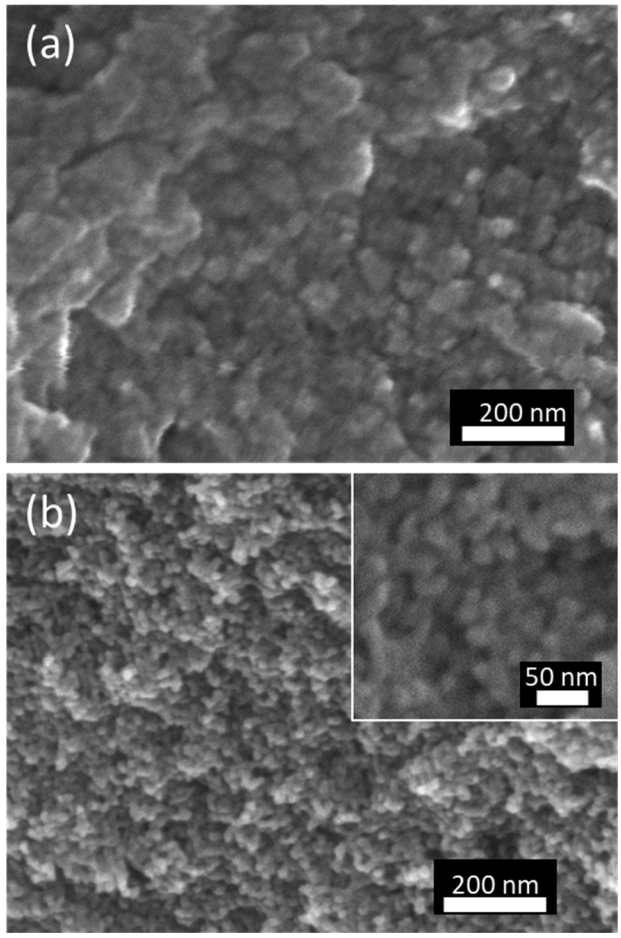

Figure 3. SEM micrograph of a monolith prepared with 20 kg mol^{-1} PEO-CTA (PEO-CTA:S/DVB = 8:17) and 2 kg mol^{-1} hPEO additive (hPEO:PEO-CTA = 1:2), (a) after hPEO release and (b) after etching all remaining PEO using HI. The inset in (b) shows an image at higher magnification.

4:17, 8:17, or 12:17) of PEO-CTA relative to the S/DVB mixture. Thus, in each case, the monoliths contain a larger fraction of total PEO and smaller fraction of the S/DVB going from hPEO:PEO-CTA mass ratios of 1:5 to 1:2 to 1:1. For example, in the case of the 1:1 hPEO:PEO-CTA with PEO-CTA:S/DVB = 8:17 sample, the monolith should contain about 52 wt % of an S/DVB derived matrix as compared to 68 wt % in the base PIMS mixture. Nonetheless, the constant CTA:monomer ratios made the chemistry of polymerization consistent and allowed us to investigate the effect of hPEO addition independently. Upon blending with these various levels of 2000 g/mol hPEO, the primary SAXS peaks for the monoliths prior to etching did not shift to a lower wavevector, which implies no significant expansion of domain spacing, for all but the highest loading (1:1 hPEO:PEO-CTA), as shown in Figure 2. After the hPEO release, the domain spacing of the hPEO:PEO-CTA = 1:1 sample reduced to a similar value to that of the unloaded sample (hPEO:PEO-CTA) and other lower hPEO loadings. It suggests only at high loading, hPEO swelled the PEO domain significantly. However, other PIMS studies found the additives in their swellable domains (ionic liquids in PEO,[30] hPEOs in PLA,[38] and hPLAs in PLA[39]) increased the domain spacing easily. Two factors contribute to this limited swelling phenomenon for blending the same homopolymer with the corresponding block. The first is

https://dx.doi.org/10.1021/acsabm.0c00228
ACS Appl. Bio Mater. 2020, 3, 3236−3247

Table 1. Summary of Nitrogen Sorption Results for HI-Etched PIMS Monoliths

sample	hPEO (wt%)	PEO-CTA (wt%)	S/DVB (wt%)	M_{hPEO} (g mol^{-1})	M_{CTA} (g mol^{-1})	surface area (m^2/g)	pore volume (mL/g)	pore width (nm)[b]	d (nm)[c]
PEO-20k-0 etched	0	32	68	--	20 000	207	0.40	7.8	20
PEO-20k-1 etched	24	24	52	2000	20 000	198	0.43	8.4	25 (18)
PEO-20k-2 etched	14	28	59	2000	20 000	196	0.40	8.1	19 (19)
PEO-20k-3 etched	6	30	64	2000	20 000	207	0.41	8.1	20 (18)
PEO-20k-4 etched[a]	14	28	59	200	20 000	180	0.34	7.8	19 (19)
PEO-20k-5 etched	14	28	59	20 000	20 000	214	0.54	10.3	22 (21)
PEO-10k-1 etched	14	28	59	2000	10 000	215	0.25	5.0	17 (14)
PEO-35k-1 etched	14	28	59	2000	35 000	207	0.57	11.8	23 (19)
PEO-20k-6 etched	9	17	74	2000	20 000	123	0.22	8.1	24 (22)
PEO-20k-7 etched	17	34	48	2000	20 000	213	0.24	5.0	19 (16)

[a]Soaked in $CHCl_3$ before etching. [b]Calculated from QSDFT analysis of the adsorption branches. [c]Domain spacing (d) from SAXS measurement for unetched samples; the values in parentheses are after hPEO release.

related to the asymmetric swelling for reducing chain stretching. Winey et al. found mixing a polystyrene homopolymer (hPS) with a poly(styrene)-*b*-poly(isoprene) (PS-*b*-PI) block polymer leads to a smaller lamellar spacing than pure copolymer when both the concentration and molar mass of hPS are low.[40] As the PS layer expands, the PI domain tends to expand laterally and decrease thickness axially at the same time. The axial contraction is favored by the relaxation of the strong chain stretching of PI. Although the morphology obtained by PIMS is a nonequilibrium state, this phenomenon could lead to the elongation of interpenetrated channel-like P(S-*co*-DVB) domains or higher levels of domain branch points to absorb the additional PEO volume during the simultaneous microphase separation/morphology freezing process and thus maintain the total domain spacing. This general preservation of domain spacing was also observed for the 200 g/mol hPEO blends in the 1:2 hPEO:PEO-CTA case (Figure 2b).

A second factor contributing to the relatively constant domain spacing upon hPEO addition is the crystallization of PEO in these blended monoliths.[41−43] The degree of crystallinity of PEO in monoliths is listed in Table S1, which was determined by crystallinity (X_c) = ΔH_m (measured)/ΔH_m (100%), where ΔH_m (measured) and ΔH_m (100%) are the heat of melting for PEO in monoliths measured from DSC (see Figure S5), calculated based on the PEO content in monoliths before and after release and that of 100% crystalline PEO (196.8 J/g), respectively. The addition of 2000 g/mol hPEO to the pure block polymer monolith formulation (PEO-CTA:S/DVB = 8:17, 20 kg/mol PEO-CTA) increased the overall PEO crystallinity from 39 to 62% in the hPEO:PEO-CTA = 1:1, consistent with the previous research on a poly(ethylene oxide)/poly(2-vinylpyridine)- *b*-(ethylene oxide) (PEO/P2VP-*b*-PEO) blend.[44] The higher crystallinity indicates PEO in the confined microdomain has a higher density upon addition of hPEO (i.e., although the overall mass fraction of PEO in the blended monoliths is higher, the overall volume fraction may remain unchanged from the base PIMS mixture). Assuming only the density change is responsible for the unaffected morphology due to the unchanged volume fraction of PEO, its density was increased by 12 and 31% for the hPEO:PEO-CTA = 1:5 and 1:2 samples, respectively.

Table 1 summarizes the N_2 sorption results of HI-etched monoliths. The BET surface area, pore volume, and mean pore width calculated from quenched solid density functional theory (QSDFT) analysis of the adsorption branches are very close among the samples with different hPEO loadings. The absence of a change in porous structure with increased hPEO loading implies the crystallinity factor might be dominant for their similar domain spacing compared to the asymmetric swelling. Generally, these data in Table 1 show the lack of significant domain dilation in most of the blended samples as manifested in SAXS. However, in the hPEO:PEO-CTA = 1:1/hPEO = 2000 g/mol case (Figure 2a), we did observe a slight shifting of q to a lower value by SAXS.

Effect of hPEO Molar Mass. In the hPEO:PEO-CTA = 1:2/PEO-CTA = 20 kg/mol cases, q shifted to a larger domain spacing when the molar mass of hPEO increased (Figure 2b). The influence of the molar mass of hPEO is also reflected on the porosity of the etched monoliths, as the pore size grew by 2.5 nm and the pore volume was 59% larger when the molar mass increased from 200 (PEO-20k-4 etched[a] in Table 1) to 20 000 (PEO-20k-5 etched in Table 1) g/mol.

Effect of PEO-CTA Molar Mass. Figure 4a shows the SAXS principle scattering peak shifted to a lower q (larger spacing) when the molar mass of PEO-CTA increased as expected based on our previous work (solid lines in Figure 4a).[45] The addition of 2000 g/mol hPEO at the hPEO:PEO-CTA = 1:2 condition did not lead to significant domain dilation in the 35 kg/mol PEO-CTA case (like the 20 kg/mol PEO-CTA), but some domain expansion was observed with the 10 kg/mol PEO-CTA (dashed lines in Figure 4a). Interestingly, after the release, the domain spacing of the 10 kg/mol PEO-CTA sample returned to its unblended state, consistent with a driving force to alleviate the osmotic stress from hPEO swelling. Complementary N_2 sorption results on these HI-etched monoliths show the pore size increased from 5.0 nm for the 10 kg/mol PEO-CTA (PEO-10k-1 etched in Table 1), to

https://dx.doi.org/10.1021/acsabm.0c00228
ACS Appl. Bio Mater. 2020, 3, 3236−3247

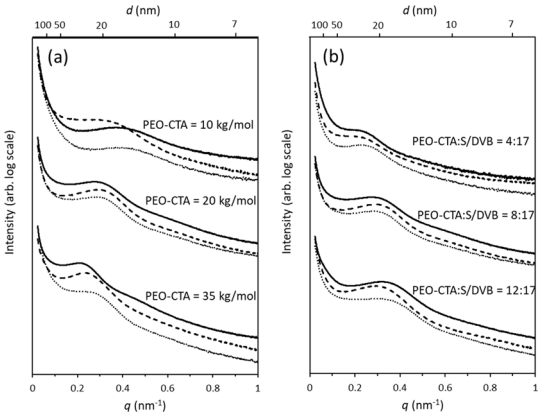

Figure 4. (a) Small-angle X-ray scattering of PEO-*b*-P(S-*co*-DVB) monoliths prepared with (a) different PEO-CTA molar masses (solid lines, domain spacing, d = 14, 20, and 33 nm from top to bottom) and same PEO-CTA:S/DVB (8:17). Dashed lines indicate samples containing 2000 g mol^{-1} of hPEO with the loading of hPEO:PEO-CTA = 1:2 (d = 17, 19, and 23 nm from top to bottom). Dotted lines indicate the samples after hPEO release (d = 14, 19, and 19 nm from top to bottom). (b) Different PEO-CTA:S/DVB (solid line, d = 24, 20, and 17 nm from top to bottom) and same molar masses (20 kg mol^{-1}). Dashed lines indicate samples containing 2000 g mol^{-1} of hPEO with the loading of hPEO:PEO-CTA = 1:2 (d = 24, 19, and 19 nm from top to bottom). Dotted lines indicate the samples after hPEO release (d = 22, 19, and 16 nm from top to bottom).

8.1 nm for the 20 kg/mol PEO-CTA (PEO-20k-2 etched), to 11.8 nm for the 35 kg/mol PEO-CTA at hPEO:PEO-CTA = 1:2 (PEO-35k-1 etched).

Effect of PEO-CTA:S/DVB. Figure 4b suggests the increased weight fraction of 20 kg/mol PEO-CTA in the polymerization mixture resulted in smaller overall domain spacings when in the base formulation without hPEO (solid lines) or when using hPEO:PEO-CTA = 1:2 and 2000 g/mol hPEO. Interestingly, N_2 sorption results of the HI-etched monoliths indicate the pore volume of the 12:17 PEO-CTA:S/DVB monolith with hPEO:PEO-CTA = 1:2 and 2000 g/mol hPEO (PEO-20k-7 etched in Table 1) was only 0.24 mL/g, much lower than the expected volume, given the initial weight fraction of PEO-CTA. This value was close to 0.22 mL/g of the 4:17 PEO-CTA:S/DVB sample (PEO-20k-6 etched). Additionally, the pore size decreased to 5 nm. One explanation is the partial pore collapse during the etching process, giving morphological information that may not be representative of the as-synthesized monolith. The fewer cross-links relative to PEO and the thinner P(S-*co*-DVB) domain may have reduced the stiffness of the matrix, leading to pore collapse.

In summary, we synthesized nanostructured polymer monoliths through a PIMS process from mixtures containing PEO-CTA, S/DVB, and hPEO. The expected disordered bicontinuous phase-separated morphology was present in all the PIMS monoliths as revealed by SAXS analysis, along with N_2 sorption experiment and SEM after removing the PEO domain. To investigate the influence of hPEO blending on the morphology of monoliths, we varied the loading and molar mass of hPEO while locking the mass ratios of PEO-CTA to S/DVB in the base PIMS mixtures in order to minimize impacts on the styrene/DVB polymerization. The most striking observation is the lack of dramatic morphological differences among most samples upon loading, until the amount of hPEO or its molar mass was high enough to be identical to PEO-CTA. We rationalize this phenomenon with the asymmetric swelling and crystallization of PEO. The molar mass of PEO-CTA and its ratio with respect to monomers had more anticipated impacts on the nanostructure as previously explored in PIMS systems. Higher PEO-CTA molar mass and lower weight fraction in the polymerization mixture led to larger domain spacings. These trends remained with hPEO blending.

Release Kinetics Study. We first studied release kinetics of samples prepared with different hPEO loadings using the 20 kg/mol PEO-CTA. As shown in Figure 5, all the experiments were carried out three times with replicate monoliths, and a high level of reproducibility was achieved. Most of the hPEO was released after 24 h in all cases. Some samples released PEO species in amounts greater than preloaded hPEO during the preparation. This discrepancy increased with the percentage of PEO-CTA, and we hypothesized that the functional PEO that was not incorporated into the network was released along with the blended hPEO. We analyzed an aliquot taken from release experiment for a monolith prepared with 2000 g/mol hPEO (hPEO:PEO-CTA = 1:2) and 20 kg mol^{-1} PEO-CTA (PEO-CTA:S/DVB = 12:17) using aqueous SEC. As shown in Figure S6a, besides the main 2000 g/mol hPEO peak, a small shoulder appears at a lower retention time and could be associated with PEO-CTA that was not incorporated into the monolith or was from PEO that was not fully functionalized with CTA. The solid mixture was obtained by evaporating water and analyzed using THF SEC. Several high molar mass species can be seen from the SEC trace (Figure S6b), which is linked to PEO-CTA or branched PEO-*b*-PS block polymers

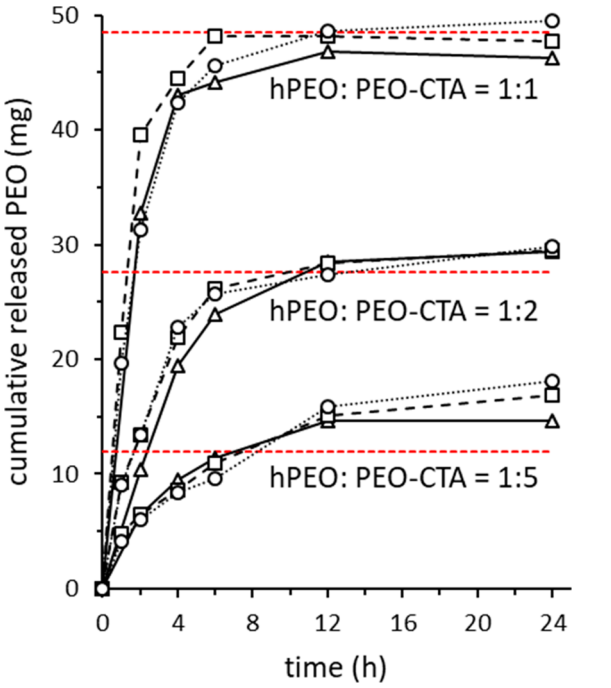

Figure 5. Cumulative released masses of hPEO vs time from PEO-*b*-P(S-*co*-DVB) monoliths prepared with 2 kg mol^{-1} hPEO homopolymer additive and 20 kg mol^{-1} PEO-CTA (PEO-CTA:S/DVB = 8:17). The mass ratios of hPEO to PEO-CTA are 1:1, 1:2, and 1:5. The solid, dashed, and dotted dark lines represent three runs for each monolith of different compositions. The corresponding initial hPEO loadings are indicated as red dashed lines.

https://dx.doi.org/10.1021/acsabm.0c00228
ACS Appl. Bio Mater. 2020, 3, 3236−3247

that were not effectively incorporated into the monolith. The ^{1}H NMR spectrum for the released mixture in $CDCl_3$ confirmed the presence of the CTA group (see Figure S7). In combination, we conclude that the released PEO species from the monoliths could contain part of unfunctionalized PEO, unreacted PEO-CTA, or a small amount of PEO-*b*-PS oligomers. However, PS peaks are not observed in the NMR spectrum, making the release of PEO-*b*-PS oligomers unlikely. After hPEO release, the SAXS patterns of all the monoliths exhibited no significant change in the position of the principal scattering peak for the corresponding prerelease monoliths, except that the highest loading sample (hPEO: CTA = 1:1) shifted back to the same position as without hPEO loading (Figure 2a). Although the reason is not clear, this unexpected result might be attributed to the abrupt removal of a large amount of homopolymer, creating an osmotic stress upon release, which might compromise the integrity of the morphology.

The release kinetics of hPEO from PIMS monoliths were fitted to a model for a cylindrical monolithic drug delivery system.[46] The release at infinite time (M_∞) was obtained as the mass loss of monoliths after repetitive washing with deionized water for at least 48 h. Fick's second law of diffusion for this geometry leads to eq 1, describing the cumulative amount of drug released as a function of time

$$\frac{M_t}{M_\infty} = 1 - \frac{32}{\pi^2}\sum_{n=1}^{\infty}\frac{1}{q_n^2}\exp\left(-\frac{q_n^2}{R^2}Dt\right)\cdot\sum_{p=0}^{\infty}\frac{1}{(2p+1)^2}\exp\left(-\frac{(2p+1)^2\pi^2}{H^2}Dt\right) \quad (1)$$

where D is the apparent diffusion coefficient of hPEO in monoliths; R and H denote the radius and height of the cylindrical monolith respectively; and q_n is the n^{th} root of the Bessel function of the first kind of order zero. It is worth noting that this model was originally developed for a homogeneous bulk monolithic device, different from our heterogeneous nanostructured system. But our tablet-like monoliths still fulfill the fundamental assumption that the preloaded compound uniformly distributed in its depot (nanodomain or whole monolith) releases through the surface of the cylinder at all directions. The macroscopic features involved in this model (radius and height of monoliths) can be separated from nanostructures, whose impact is incorporated in eq 2 as discussed in the following paragraph.

Figure 6 shows the fitting of hPEO release data to the model was good with an r^2 higher than 0.96. The release rate decreased with time because of a longer diffusion path and lower concentration of hPEO on the surface.[47] From the equation, we can calculate the apparent diffusion coefficient of hPEO in the monoliths, which are shown in Table 2. Considering the nanostructural heterogeneity of the monoliths, we used eq 2 to calculate the effective diffusion coefficient D^* of hPEO in PEO-rich domains of the monoliths where hPEO chains actually diffuse, by taking the surface area fraction f_s and tortuosity τ of PEO domain into account

$$D = \frac{f_s}{\tau}\cdot D^* \quad (2)$$

where D^* is the hPEO diffusion coefficient in the PEO-rich domain; f_s is the surface area fraction of PEO, which is assumed to be the same as the volume fraction of the PEO domain in the whole monoliths, f_v, estimated from pore volume determined by N_2 sorption; τ is the tortuosity of PEO

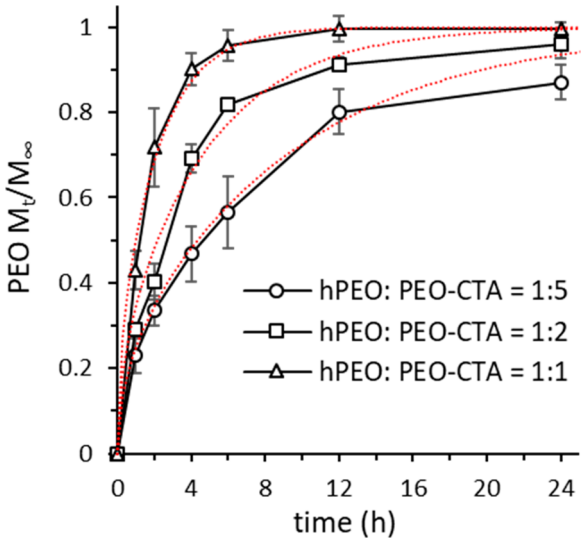

Figure 6. Ratio of cumulative released masses of hPEO at different times (M_t) (averaged from three runs) to total release at infinite time (M_∞) from PEO-*b*-P(S-*co*-DVB) monoliths prepared with 2 kg mol^{-1} hPEO and 20 kg mol^{-1} PEO-CTA (PEO-CTA:S/DVB = 8:17). The ratios of hPEO to PEO-CTA are 1:1, 1:2, and 1:5. The fits using eq 1 are represented as dashed red lines.

domain ranging from 1.5 to 3 for cocontinuous networks.[30] As a result, D^* for hPEO was given as a range estimated with τ (1.5−3). Eq 2 is adopted from the equation used by Schulze et al.[29] and Chopade et al.[31,48] to convert the observed conductivity of ionic-liquid-containing PIMS electrolyte membranes to the inherent conductivity in a homogeneous electrolyte/PEO/ionic-liquid system without PS and a nanostructure. In their work, the tortuosity parameter (τ) accounts for the relatively longer path ions must travel compared to the distance between the electrodes. In the present system, the actual diffusion path of loaded hPEO is also prolonged by this tortuosity, resulting from the cocontinuous morphology. Additionally, for the PIMS electrolyte membrane, the conductivity was corrected by the volume fraction of the conducting phase (f_c), because only that part of membranes allowed ions to reside and pass through. In a drug delivery PIMS monolith, the outer surface is the only location that hPEO releases to solution happens. So, the area fraction of the available PEO channel opening on the surface should be included into the equation, too. We assume the nanostructure in the whole monolith is uniform. In any infinitesimally thin slice (dL) across the monolith, including the surface (f_s), the fraction of the PEO domain should be equal to its total volume fraction (f_v).

Effect of hPEO Loading. Table 2 shows higher hPEO loading led to higher diffusion coefficients (D^*). N_2 sorption results manifest that pore volumes and sizes of these monoliths with different loadings (hPEO:PEO-CTA = 0, 1:5, 1:2, and 1:1) were almost identical. Therefore, higher hPEO loading resulted in higher density (i.e., concentration) and an increased degree of crystallinity as shown in Table S1. But this trend of diffusivity cannot be explained by a higher initial concentration from higher loading, because there is no concentration term in eq 1, which is normalized with M_∞/M_t. We hypothesize that the loading of hPEO disrupted the morphology of the PEO domain once exposed to water. As the hPEO of higher density leached out, it left more voids that allowed faster diffusion for

https://dx.doi.org/10.1021/acsabm.0c00228
ACS Appl. Bio Mater. 2020, 3, 3236−3247

Table 2. Diffusion Parameters of 2 and 20 kg mol^{-1} PEO Homopolymer in PIMS Monoliths

hPEO:CTA[a]	M_{hPEO} (g mol^{-1})	D (cm^2/s) (× 10^{-8})	r^2	D^* (cm^2/s) (× 10^{-8})[b]	D_0 (cm^2/s) (× 10^{-8})[c]	D^*/D_0
1:1	2000	7.0	0.98	23.3∼46.6	107	0.22∼0.44
1:2	2000	3.2	0.96	11.4∼22.8	107	0.11∼0.21
1:5	2000	1.6	0.97	5.6∼11.2	107	0.05∼0.10
1:2	20 000	1.6	0.96	4.4∼8.8	58	0.08∼0.15

[a]PEO-*b*-P(S-*co*-DVB) monoliths prepared with 2 or 20 kg mol^{-1} PEO homopolymer additive and 20 kg mol^{-1} PEO-CTA (PEO-CTA:S/DVB = 8:17). [b]Estimate f_s from pore volume determined by N_2 sorption and assume τ to be between 1.5 and 3.[30] [c]Self-diffusion coefficient (D_0) of 2 kg/mol[49] and 20 kg/mol[50] of PEO in water.

the following hPEO inside the monoliths. Higher crystallinity led by higher loading could further drive the release of hPEO, owing to a larger density change associated with the abrupt transformation to a swollen amorphous state.

We propose that the structure of the PEO domains in monoliths was similar to that of hydrogels, despite the fact that PEO chains as middle blocks were immobilized by being tethered to the PS/P(S-*co*-DVB) interface with a loop or bridge arrangement, instead of cross-linking. The ratio of the diffusion coefficient (D^*) in materials to the self-diffusion coefficient of free hPEO molecules in water (D_0) is commonly used as an indicator of the diffusivity of hydrogels.[51] Hagel et al. reported a PEO-based hydrogel system made with 20 kg mol^{-1} poly(ethylene glycol)-diacrylate (PEG-DA) and studied the diffusion rate of dextran in the hydrogels.[52] They found D^*/D_0 ranges from 0.35 to 0.6 for the dextran with a hydrodynamic radius close to 2 kg mol^{-1} hPEO (1.36 nm[53]). Compared to the PEG hydrogel, hPEO in our monoliths had a lower diffusivity (D^*/D_0). This can be explained by the confinement caused by the rigid P(S-*co*-DVB) matrix that limited the swelling of the PEO domain, comparable to the effect of reducing the mesh size of PEO for solutes to diffuse in swellable hydrogels. Indeed, no significant macroscopic swelling of monoliths was observed in water during our release experiments.

Effect of hPEO Molar Mass. In samples with hPEO to PEO-CTA = 1:2, the hPEO was released from monoliths more slowly when the molar mass of hPEO increased from 2 to 20 kg/mol (Figure 7). The apparent diffusion coefficient (D) of 20 kg/mol hPEO was a half of 2 kg/mol with the same hPEO:PEO-CTA ratio (see Table 2). Although the pore volume and pore width were higher for 20 kg/mol hPEO (see Table 1), indicating a larger PEO domain, the bigger hydrodynamic radius of 20 kg/mol hPEO led to more friction inside the PEO channel and slowed its diffusion (i.e., lower D_0). When we normalized the diffusion coefficient (D^*) corresponding with the 20 kg/mol PEO with its self-diffusion coefficient (D_0), this ratio, D^*/D_0, which reflects the intrinsic media diffusivity, was closer to that of 2 kg/mol hPEO with the same hPEO:PEO-CTA = 1:2 (Table 2). It was expected that hPEO with the lowest molar mass of 200 g/mol would have the highest release rate. However, the final released mass of 200 g/mol hPEO was less than the higher molar mass hPEO and reached a maximum that was less than half of the original hPEO loading after 24 h. No more hPEO could be leached out even after 3 days in water, until the monolith was soaked in chloroform, which swelled the P(S-*co*-DVB) domain, upon which the remaining hPEO was released. We surmise that the residual 200 g/mol was trapped in the P(S-*co*-DVB) domain, because their low molar mass made mixing with the hydrophobic domain less unfavorable. When Flory–Huggins

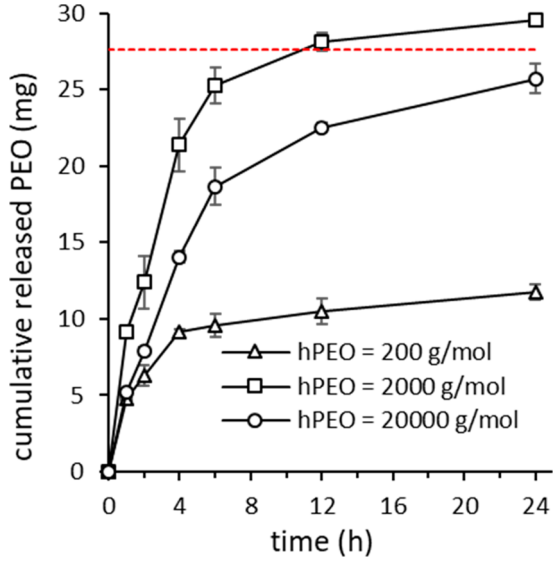

Figure 7. Cumulative released masses of hPEO vs time from PEO-*b*-P(S-*co*-DVB) monoliths prepared with hPEO homopolymer additives of different molar masses and 20 kg mol^{-1} PEO-CTA (PEO-CTA:S/DVB = 8:17). The mass ratios of hPEO to PEO-CTA are 1:2 in all cases. The initial hPEO loading (27.6 mg) is indicated as a red dashed line.

theory is applied to polymer mixing, the free energy of mixing (ΔG_{mix}) can be expressed as

$$\frac{\Delta G_{mix}}{kT} = \chi\phi_1\phi_2 + \frac{\phi_1}{N_1}\ln\phi_1 + \frac{\phi_2}{N_2}\ln\phi_2 \quad (3)$$

where k is Boltzmann's constant; T is the temperature; χ is the Flory–Huggins interaction parameter; ϕ_1 and N_1 are the volume fraction and degree of polymerization of polymer 1; and ϕ_2 and N_2 are the volume fraction and degree of polymerization of polymer 2. The last two items in eq 3 describe the entropic contribution from random mixing of two polymers. Because ϕ_1 and ϕ_2 are less than 1, the entropy of mixing will always be positive.[54] A lower molar mass of hPEO (i.e., lower N) led to a higher entropy gain for mixing with PS. It alleviated the unfavorable enthalpy of mixing (positive χ) and resulted in the partial compatibility of 200 g/mol hPEO in the PS matrix. The PEO trapping in the cross-linked PS matrix was also observed by Saba et al.[38] They found even after etching the PLA domain by base, 11 wt % of 35 kg mol^{-1} residual PEO was still found in the mesoporous P(S-*co*-DVB) monolith, which could be accessed and removed by exposure to chloroform.

Effect of PEO-CTA Molar Mass. The effect of the molar mass of the starting PEO-CTA on the release rate of 2 kg/mol hPEO with the same loading was interestingly negligible

https://dx.doi.org/10.1021/acsabm.0c00228
ACS Appl. Bio Mater. 2020, 3, 3236–3247

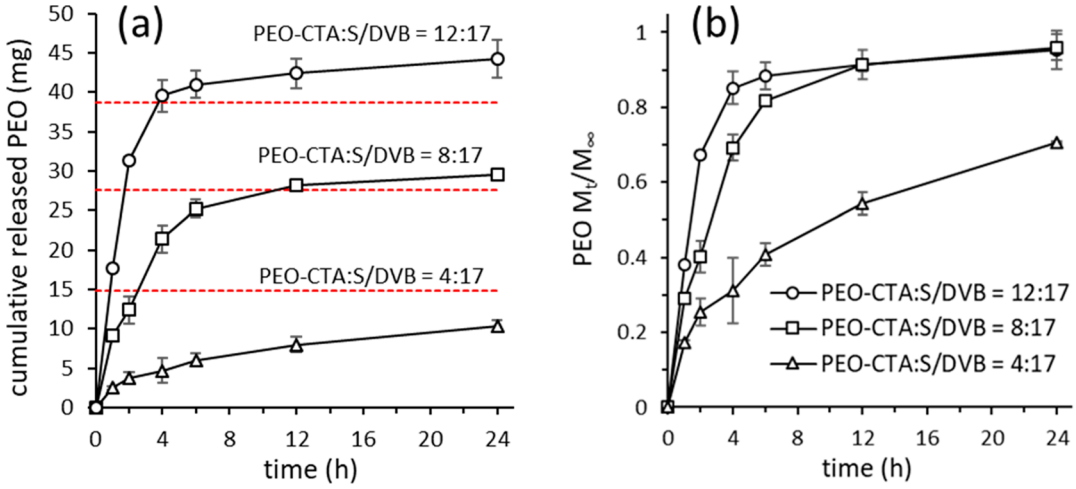

Figure 8. (a) Cumulative released masses of hPEO vs time and (b) the ratio of cumulative released masses of hPEO at different times (M_t) to total release at infinite time (M_∞) from PEO-*b*-P(S-*co*-DVB) monoliths prepared with 2000 g mol^{-1} of hPEO homopolymer additives and 20 kg mol^{-1} PEO-CTA of different mass ratios in the prepolymer mixture (PEO-CTA:S/DVB). The mass ratios of hPEO to PEO-CTA are 1:2 in all cases. The corresponding initial hPEO loadings are indicated as red dashed lines.

(Figure S8), despite the large differences between 10, 20, and 35 kg mol^{-1} PEO-CTA on domain spacing (Table 1 and Figure 4a). This result implies the size of single PEO diffusion channel had little impact on the release kinetics for 2 kg/mol hPEO with the range of domain sizes explored. The increased entanglement from increased molar mass could be mediated by domain dilation and hydration.

Effect of PEO-CTA:S/DVB. However, when the mass ratio of 20 kg mol^{-1} PEO-CTA to monomer was decreased to 4:17, the release rate of the corresponding monolith was significantly lower than that of 8:17 and 12:17 PEO-CTA samples at hPEO:PEO-CTA = 1:2 (Figure 8). The fraction of hPEO:PEO-CTA in these samples was not the same, and as a result, the area of PEO domain present on the surface available for hPEO diffusion was decreased, which could be responsible for the lower release rate in the case of PEO-CTA:S/DVB = 4:17. Previous work has also observed the loss of domain cocontinuity and more isolated spherical domains when the fraction of macro-CTA decreases, which might contribute to the slow and incomplete release in 4:17 PEO-CTA:S/DVB as well.[32,45]

In summary, we studied the release kinetics of hPEO in the nanostructured monoliths with a controlled shape and size to eliminate geometric effects and focus on the influence of different compositions. In all cases, the release rate decreased with time. Some amount of unreacted PEO-CTA leached out along with hPEO. Fitting the release data into a model for a cylindrical monolithic system reveals that the diffusion coefficients (D^*) of 2 kg/mol hPEO were lower than that of dextran with a similar hydrodynamic radius in a PEG-DA hydrogel system, which can be attributed to the limited swelling of PEO domains confined by the rigid PS matrix. We also found despite the morphological similarity, the higher hPEO loading led to higher diffusion coefficients due to the larger voids created by diffusion in the monoliths. The higher molar mass hPEO (20 kg/mol) diffused more slowly as expected. But when the size of hPEO decreased to 200 g/mol, it could be trapped into the PS domain and thus was not fully released. The different domain sizes resulting from different molar masses of PEO-CTA did not significantly impact the release rate. Decreasing the weight fraction of PEO-CTA in the prepolymer mixture decreased the release rate because of the smaller area of the PEO domain present on the surface and decreased domain cocontinuity. The above results suggest that the release rate did not depend on the dimension of the PEO diffusion channels but the volume fraction in the monolith. Meanwhile, the amount and nature of loaded molecules also dictated their release behaviors.

Nanostructured Microneedles and Nanostructure-Promoted PLA Degradation. One drawback of implantable monoliths as we discussed so far in this paper is that they require invasive surgery to implant and remove at the end of the therapy. To overcome this limitation, an emerging solution is to utilize microneedle patches to deliver drugs transdermally.[55] We took advantage of the well-established microfabrication technologies and easy-to-tailor in situ microphase separation/cross-linking process to develop novel microneedles with both a desirable macroscopic geometry that enables efficient and painless administration and a nanostructure that facilitates controlled transdermal drug release (see Figure S9). The successful fabrication is demonstrated by the SEM images of microneedle arrays prepared with both 30 kg mol^{-1} PLA-CTA (PLA-CTA:S/DVB = 4:17) (Figure 9a) and 20 kg mol^{-1} PEO-CTA (PEO-CTA:S/DVB = 4:17) with 2 kg mol^{-1} hPEO (hPEO:PEO-CTA = 1:2) (Figure 9b). The dimensional parameters of all the microneedles were the same, because they were replicated from the same SU8 master structure. The height of these microneedles was about 450 μm, which could penetrate the skin barrier for effective drug delivery but would not reach the nerve system to cause pain. They had a base diameter of 80 μm and a tip diameter of 20 μm. The removal of the PLA domain with NaOH did not alter the macroscopic geometry, including the height and the tip diameter of microneedles as evidenced by Figure 9c, while the SEM image at high magnification reveals the nanoporous structure in microneedles (see Figure 9d). These are the only nanoporous microneedles that have ever been reported apart from hollow microneedles with a single bore. The fabrication method and more discussion can be found in Supporting Information. Under the same conditions, the intrinsic diffusion coefficients of hPEO species in PEO-CTA microneedles should be similar to the cylindrical

https://dx.doi.org/10.1021/acsabm.0c00228
ACS Appl. Bio Mater. 2020, 3, 3236−3247

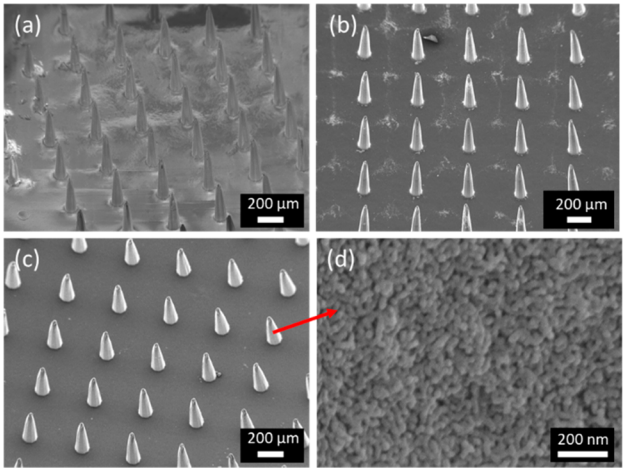

Figure 9. SEM micrograph of a PIMS microneedle patch prepared with (a) 30 kg mol^{-1} PLA-CTA (PLA-CTA:S/DVB = 4:17) and (b) 20 kg mol^{-1} PEO-CTA (PEO-CTA:S/DVB = 4:17) with 2 kg mol^{-1} hPEO (PEO:CTA = 1:2); PLA-CTA microneedles after etching at (c) low and (d) high magnification.

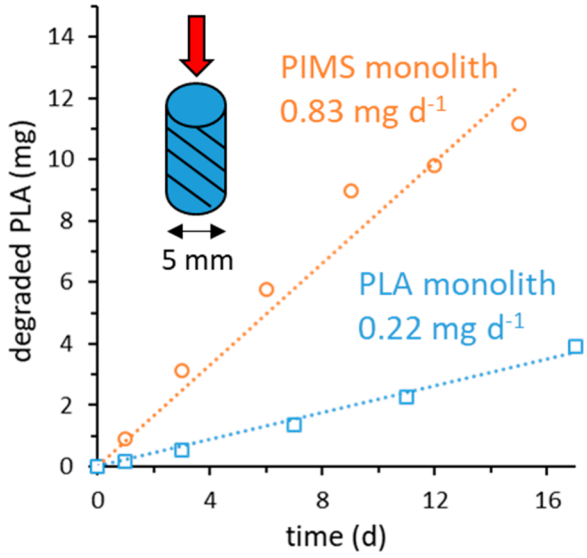

Figure 10. Masses of degraded PLA vs time from monoliths prepared with 32 wt % of 30 kg mol^{-1} PLA-CTA and S/DVB (○) and 30 kg mol^{-1} PLA-CTA alone (□) in 1 M NaOH aqueous solution. Both monoliths are cylindrical with a diameter of 5 mm. Only their tops were open to basic solution, while the rest of surface was covered by Parafilm.

tablets that we measured in the present work. However, the release profiles, which are geometry dependent, must be different, and this is a topic for future research.

We have reported diffusion-based release from the PEO domain in nanostructured monoliths. On the other hand, degradation-based drug delivery is also a major pathway and worth to investigate in our PIMS monoliths. Among the common biodegradable matrix materials, poly(lactide) (PLA) is one of the most important polymers in the medical field due to its excellent biocompatibility, mechanical strength, and biodegradability with nontoxic hydrolysis products. PLA-based biomaterials find a broad spectrum of clinical applications such as tissue engineering, drug delivery, and implants for bone fixation.[56] Nevertheless, the slow degradation of PLA is undesirable in some circumstances. Various approaches have been employed to control the degradation rate, including using racemic lactide to suppress crystallinity, copolymerization or blending with less hydrophobic polymers, additives, and irradiation.[57] We studied the degradation of microphase-separated PLA in nanostructured monoliths prepared by the PIMS process. Their degradation rate, normalized by 32 wt % of PLA in a PIMS monolith of the same mass as the bulk monolith, was found to be 10-fold faster than bulk PLA under the same basic hydrolysis conditions (see Figure 10). We speculate the cocontinuous PLA 3D network might create a "rough" corroding front, exposing more degradable sites for hydroxide to attack. Interested readers are referred to the Supporting Information for detailed experiment design and analysis. This finding opens a new door to accelerate PLA degradation with the promotion of nanostructure. Although in this work, we conducted a degradation test with a basic solution to shorten the experimental time, we expect this effect would also apply to PLA degradation under physiological conditions. Hence, we hypothesize it could potentially be used to regulate the release of drugs embedded in PLA nano-domains when implanted into human body. Their degradation rates and release behaviors under physiological condition as a function of tunable nanostructure could be the subject of future research efforts.

CONCLUSION

Nanostructured polymer monoliths were synthesized through a polymerization-induced microphase separation process from PEO-CTA, S/DVB, and PEO homopolymers. A typical disordered bicontinuous morphology was present in all the monoliths, where the PEO domain acted as both the reservoir and diffusion channels for preloaded hPEO. We found hPEO did not increase the length scale of the bicontinuous morphology significantly when its loading and molar mass did not exceed that of PEO-CTA. The influence of weight fraction and molar mass of PEO-CTA on the morphology met our expectation based on the composition of the resulting copolymers. We then studied the release behavior of hPEO from the monoliths and fitted the kinetic data to a theoretical model for cylindrical monolithic systems. The diffusion coefficient of hPEO increased at higher loading and lower molar mass of hPEO. A comparison to the PEG hydrogels suggests PIMS monoliths retarded the diffusion in the same conditions, because the PS matrix prevented the swelling of PEO diffusion channels. The molar mass of PEO-CTA did not affect the release, while increasing the ratio of the PEO-CTA to S/DVB mixture presented more PEO domain on the monolith surface and increased the release rate in turn. In conclusion, nanostructured PIMS monoliths show promise as a scaffold for biomedical implants to achieve tailored drug release by tuning fabrication parameters. Furthermore, we demonstrated the synthesis process for monoliths could be applied to fabricate nanostructured microneedle arrays aimed at sustained painless drug administration and discovered that the PLA degradation could be dramatically accelerated by the nanostructure, which encourages us to develop PLA-based PIMS implants for degradation-induced drug release in the future.

https://dx.doi.org/10.1021/acsabm.0c00228
ACS Appl. Bio Mater. 2020, 3, 3236−3247

■ ASSOCIATED CONTENT

Supporting Information

The Supporting Information is available free of charge at https://pubs.acs.org/doi/10.1021/acsabm.0c00228.

Experimental details, additional characterization information (SEC, NMR, N_2 sorption, and DSC) and release kinetic data as well as more discussion on microneedles and nanostructure-promoted PLA degradation (PDF)

■ AUTHOR INFORMATION

Corresponding Author

Marc A. Hillmyer − *Department of Chemistry, University of Minnesota, Minneapolis, Minnesota 55455-0431, United States;* orcid.org/0000-0001-8255-3853; Email: hillmyer@umn.edu

Author

Yihui Xie − *Department of Chemistry, University of Minnesota, Minneapolis, Minnesota 55455-0431, United States;* orcid.org/0000-0003-0159-9011

Complete contact information is available at: https://pubs.acs.org/10.1021/acsabm.0c00228

Notes

The authors declare no competing financial interest.

■ ACKNOWLEDGMENTS

This work was supported in part by the National Science Foundation (DMR-1609459 and DMR-2003454). SAXS data were obtained at the APS, Sector 5 (DuPont−Northwestern−Dow Collaborative Access Team, DND-CAT) and Sector 12. DND-CAT is supported by The Dow Chemical Company, E. I. DuPont de Nemours & Co., and Northwestern University. Use of the APS, an Office of Science User Facility operated for the U.S. Department of Energy (DOE), Office of Science, by Argonne National Laboratory, was supported by the U.S. DOE under Contract DE-AC02-06CH11357. Parts of this work were carried out in the Characterization Facility, University of Minnesota, which receives partial support from NSF through the MRSEC program. Portions of this work were conducted in the Minnesota Nano Center, which is supported by NSF through the National Nano Coordinated Infrastructure Network, Award Number NNCI −1542202. The authors thank Colin Peterson, Nicholas Hampu, and David Goldfeld for helpful input.

■ REFERENCES

(1) Siepmann, J., Siegel, R. A., Rathbone, M. J., Eds. *Fundamentals and Applications of Controlled Release Drug Delivery*; Advances in Delivery Science and Technology; Springer US, 2011.

(2) Allen, T. M. Drug Delivery Systems: Entering the Mainstream. *Science* **2004**, *303* (5665), 1818−1822.

(3) Danhier, F.; Feron, O.; Préat, V. To Exploit the Tumor Microenvironment: Passive and Active Tumor Targeting of Nanocarriers for Anti-Cancer Drug Delivery. *J. Controlled Release* **2010**, *148* (2), 135−146.

(4) Wang, B.; Hu, L.; Siahaan, T. J. *Drug Delivery: Principles and Applications*, 2nd ed.; Wiley Series in Drug Discovery and Development; Wiley, 2016.

(5) Bicker, J.; Alves, G.; Fortuna, A.; Falcão, A. Blood-Brain Barrier Models and Their Relevance for a Successful Development of CNS Drug Delivery Systems: A Review. *Eur. J. Pharm. Biopharm.* **2014**, *87* (3), 409−432.

(6) Timko, B. P.; Arruebo, M.; Shankarappa, S. A.; McAlvin, J. B.; Okonkwo, O. S.; Mizrahi, B.; Stefanescu, C. F.; Gomez, L.; Zhu, J.; Zhu, A.; Santamaria, J.; Langer, R.; Kohane, D. S. Near-Infrared-Actuated Devices for Remotely Controlled Drug Delivery. *Proc. Natl. Acad. Sci. U. S. A.* **2014**, *111* (4), 1349−1354.

(7) Zhang, Y.; Chan, H. F.; Leong, K. W. Advanced Materials and Processing for Drug Delivery: The Past and the Future. *Adv. Drug Delivery Rev.* **2013**, *65* (1), 104−120.

(8) Mura, S.; Nicolas, J.; Couvreur, P. Stimuli-Responsive Nanocarriers for Drug Delivery. *Nat. Mater.* **2013**, *12* (11), 991−1003.

(9) Kamaly, N.; Xiao, Z.; Valencia, P. M.; Radovic-Moreno, A. F.; Farokhzad, O. C. Targeted Polymeric Therapeutic Nanoparticles: Design, Development and Clinical Translation. *Chem. Soc. Rev.* **2012**, *41* (7), 2971.

(10) Sun, T.; Zhang, Y. S.; Pang, B.; Hyun, D. C.; Yang, M.; Xia, Y. Engineered Nanoparticles for Drug Delivery in Cancer Therapy. *Angew. Chem., Int. Ed.* **2014**, *53* (46), 12320−12364.

(11) Kesharwani, P.; Jain, K.; Jain, N. K. Dendrimer as Nanocarrier for Drug Delivery. *Prog. Polym. Sci.* **2014**, *39* (2), 268−307.

(12) Elsabahy, M.; Wooley, K. L. Design of Polymeric Nanoparticles for Biomedical Delivery Applications. *Chem. Soc. Rev.* **2012**, *41* (7), 2545−2561.

(13) Santos, A.; Sinn Aw, M.; Bariana, M.; Kumeria, T.; Wang, Y.; Losic, D. Drug-Releasing Implants: Current Progress, Challenges and Perspectives. *J. Mater. Chem. B* **2014**, *2* (37), 6157.

(14) Maulvi, F. A.; Soni, T. G.; Shah, D. O. A Review on Therapeutic Contact Lenses for Ocular Drug Delivery. *Drug Delivery* **2016**, *23* (8), 3017−3026.

(15) Padmakumar, S.; Paul-prasanth, B.; Pavithran, K.; Vijaykumar, D. K.; Rajanbabu, A.; Sivanarayanan, T. B.; Kadakia, E.; Amiji, M. M.; Nair, S. V.; Menon, D. Long-Term Drug Delivery Using Implantable Electrospun Woven Polymeric Nanotextiles. *Nanomedicine* **2019**, *15* (1), 274−284.

(16) Chen, Y.; Yang, Y.; Xian, Y.; Singh, P.; Feng, J.; Cui, S.; Carrier, A.; Oakes, K.; Luan, T.; Zhang, X. Multifunctional Graphene-Oxide-Reinforced Dissolvable Polymeric Microneedles for Transdermal Drug Delivery. *ACS Appl. Mater. Interfaces* **2020**, *12*, 352−360.

(17) Ma, G.; Wu, C. Microneedle, Bio-Microneedle and Bio-Inspired Microneedle: A Review. *J. Controlled Release* **2017**, *251*, 11−23.

(18) Ita, K. Transdermal Delivery of Drugs with Microneedles: Strategies and Outcomes. *J. Drug Delivery Sci. Technol.* **2015**, *29*, 16−23.

(19) van der Maaden, K.; Jiskoot, W.; Bouwstra, J. Microneedle Technologies for (Trans)dermal Drug and Vaccine Delivery. *J. Controlled Release* **2012**, *161* (2), 645−655.

(20) Indermun, S.; Luttge, R.; Choonara, Y. E.; Kumar, P.; du Toit, L. C.; Modi, G.; Pillay, V. Current Advances in the Fabrication of Microneedles for Transdermal Delivery. *J. Controlled Release* **2014**, *185*, 130−138.

(21) Kim, Y.-C.; Park, J.-H.; Prausnitz, M. R. Microneedles for Drug and Vaccine Delivery. *Adv. Drug Delivery Rev.* **2012**, *64* (14), 1547−1568.

(22) Li, J.; Mooney, D. J. Designing Hydrogels for Controlled Drug Delivery. *Nat. Rev. Mater.* **2016**, *1* (12), 16071.

(23) Yan, L.; Yang, Y.; Zhang, W.; Chen, X. Advanced Materials and Nanotechnology for Drug Delivery. *Adv. Mater.* **2014**, *26* (31), 5533−5540.

(24) Lee, K.; Lingampalli, N.; Pisano, A. P.; Murthy, N.; So, H. Physical Delivery of Macromolecules Using High-Aspect Ratio Nanostructured Materials. *ACS Appl. Mater. Interfaces* **2015**, *7* (42), 23387−23397.

(25) Habibi, N.; Kamaly, N.; Memic, A.; Shafiee, H. Self-Assembled Peptide-Based Nanostructures: Smart Nanomaterials toward Targeted Drug Delivery. *Nano Today* **2016**, *11* (1), 41−60.

(26) Seo, M.; Hillmyer, M. A. Reticulated Nanoporous Polymers by Controlled Polymerization-Induced Microphase Separation. *Science* **2012**, *336* (6087), 1422−1425.

(27) Seo, M.; Kim, S.; Oh, J.; Kim, S. J.; Hillmyer, M. A. Hierarchically Porous Polymers from Hyper-Cross-Linked Block Polymer Precursors. *J. Am. Chem. Soc.* **2015**, *137* (2), 600−603.
(28) Leiston-Belanger, J. M.; Russell, T. P.; Drockenmuller, E.; Hawker, C. J. A Thermal and Manufacturable Approach to Stabilized Diblock Copolymer Templates. *Macromolecules* **2005**, *38* (18), 7676−7683.
(29) Schulze, M. W.; McIntosh, L. D.; Hillmyer, M. A.; Lodge, T. P. High-Modulus, High-Conductivity Nanostructured Polymer Electrolyte Membranes via Polymerization-Induced Phase Separation. *Nano Lett.* **2014**, *14* (1), 122−126.
(30) McIntosh, L. D.; Schulze, M. W.; Irwin, M. T.; Hillmyer, M. A.; Lodge, T. P. Evolution of Morphology, Modulus, and Conductivity in Polymer Electrolytes Prepared via Polymerization-Induced Phase Separation. *Macromolecules* **2015**, *48* (5), 1418−1428.
(31) Chopade, S. A.; So, S.; Hillmyer, M. A.; Lodge, T. P. Anhydrous Proton Conducting Polymer Electrolyte Membranes via Polymerization-Induced Microphase Separation. *ACS Appl. Mater. Interfaces* **2016**, *8* (9), 6200−6210.
(32) Peterson, C.; Hillmyer, M. A. Fast Photochromic Dye Response in Rigid Block Polymer Thermosets. *ACS Appl. Polym. Mater.* **2019**, *1*, 2778−2786.
(33) Bode, C.; Kranz, H.; Fivez, A.; Siepmann, F.; Siepmann, J. Often Neglected : PLGA/PLA Swelling Orchestrates Drug Release : HME Implants. *J. Controlled Release* **2019**, *306* (January), 97−107.
(34) Kumar, S.; Singh, S.; Senapati, S.; Singh, A. P.; Ray, B.; Maiti, P. Controlled Drug Release through Regulated Biodegradation of Poly (Lactic Acid) Using Inorganic Salts. *Int. J. Biol. Macromol.* **2017**, *104*, 487−497.
(35) Maitz, M. F. Applications of Synthetic Polymers in Clinical Medicine. *Biosurface and Biotribology* **2015**, *1* (3), 161−176.
(36) El Fray, M.; Prowans, P.; Puskas, J. E.; Altstädt, V. Biocompatibility and Fatigue Properties of Polystyrene−Polyisobutylene−Polystyrene, an Emerging Thermoplastic Elastomeric Biomaterial. *Biomacromolecules* **2006**, *7* (3), 844−850.
(37) Banerjee, S. S.; Aher, N.; Patil, R.; Khandare, J. Poly(Ethylene Glycol)-Prodrug Conjugates: Concept, Design, and Applications. *J. Drug Delivery* **2012**, *2012*, 1−17.
(38) Saba, S. A.; Mousavi, M. P. S.; Bühlmann, P.; Hillmyer, M. A. Hierarchically Porous Polymer Monoliths by Combining Controlled Macro- and Microphase Separation. *J. Am. Chem. Soc.* **2015**, *137* (28), 8896−8899.
(39) Park, J.; Saba, S. A.; Hillmyer, M. A.; Kang, D.-C.; Seo, M. Effect of Homopolymer in Polymerization-Induced Microphase Separation Process. *Polymer* **2017**, *126*, 338−351.
(40) Winey, K. I.; Thomas, E. L.; Fetters, L. J. Swelling of Lamellar Diblock Copolymer by Homopolymer: Influences of Homopolymer Concentration and Molecular Weight. *Macromolecules* **1991**, *24* (23), 6182−6188.
(41) Rangarajan, P.; Haisch, C. F.; Register, R. A.; Adamson, D. H.; Fetters, L. J. Influence of Semicrystalline Homopolymer Addition on the Morphology of Semicrystalline Diblock Copolymers. *Macromolecules* **1997**, *30* (3), 494−502.
(42) Yu, C.; Xie, Q.; Bao, Y.; Shan, G.; Pan, P. Crystalline and Spherulitic Morphology of Polymers Crystallized in Confined Systems. *Crystals* **2017**, *7* (5), 147.
(43) Pitet, L. M.; Chamberlain, B. M.; Hauser, A. W.; Hillmyer, M. A. Dispersity and Architecture Driven Self-Assembly and Confined Crystallization of Symmetric Branched Block Copolymers. *Polym. Chem.* **2019**, *10* (39), 5385−5395.
(44) Araneda, E.; Leiva, A.; Gargallo, L.; Hadjichristidis, N.; Mondragon, I.; Radic, D. Crystallization Behavior of PEO in Blends of Poly(Ethylene Oxide)/Poly(2-Vinyl Pyridine)-*b*-(Ethylene Oxide) Block Copolymer. *Polym. Eng. Sci.* **2012**, *52* (5), 1128−1136.
(45) Schulze, M. W.; Hillmyer, M. A. Tuning Mesoporosity in Cross-Linked Nanostructured Thermosets via Polymerization-Induced Microphase Separation. *Macromolecules* **2017**, *50* (3), 997−1007.
(46) Siepmann, J.; Siepmann, F. Modeling of Diffusion Controlled Drug Delivery. *J. Controlled Release* **2012**, *161* (2), 351−362.
(47) Siepmann, J.; Ainaoui, A.; Vergnaud, J. M.; Bodmeier, R. Calculation of the Dimensions of Drug-Polymer Devices Based on Diffusion Parameters. *J. Pharm. Sci.* **1998**, *87* (7), 827−832.
(48) Chopade, S. A.; Au, J. G.; Li, Z.; Schmidt, P. W.; Hillmyer, M. A.; Lodge, T. P. Robust Polymer Electrolyte Membranes with High Ambient-Temperature Lithium-Ion Conductivity via Polymerization-Induced Microphase Separation. *ACS Appl. Mater. Interfaces* **2017**, *9* (17), 14561−14565.
(49) Amsden, B. Modeling Solute Diffusion in Aqueous Polymer Solutions. *Polymer* **2002**, *43* (5), 1623−1630.
(50) Palit, S.; Khajehpour Tadavani, S.; Yethiraj, A. Realization of a Stable, Monodisperse Water-in-Oil Droplet System with Micro-Scale and Nano-Scale Confinement for Tandem Microscopy and Diffusion NMR Studies. *Soft Matter* **2018**, *14* (3), 448−459.
(51) Lin, C. C.; Metters, A. T. Hydrogels in Controlled Release Formulations: Network Design and Mathematical Modeling. *Adv. Drug Delivery Rev.* **2006**, *58* (12−13), 1379−1408.
(52) Hagel, V.; Haraszti, T.; Boehm, H. Diffusion and Interaction in PEG-DA Hydrogels. *Biointerphases* **2013**, *8* (1), 36.
(53) Armstrong, J. K.; Wenby, R. B.; Meiselman, H. J.; Fisher, T. C. The Hydrodynamic Radii of Macromolecules and Their Effect on Red Blood Cell Aggregation. *Biophys. J.* **2004**, *87* (6), 4259−4270.
(54) Tambasco, M.; Lipson, J. E. G.; Higgins, J. S. Blend Miscibility and the Flory−Huggins Interaction Parameter: A Critical Examination. *Macromolecules* **2006**, *39* (14), 4860−4868.
(55) Larrañeta, E.; McCrudden, M. T. C.; Courtenay, A. J.; Donnelly, R. F. Microneedles: A New Frontier in Nanomedicine Delivery. *Pharm. Res.* **2016**, *33* (5), 1055−1073.
(56) Gupta, A. P.; Kumar, V. New Emerging Trends in Synthetic Biodegradable Polymers − Polylactide: A Critique. *Eur. Polym. J.* **2007**, *43* (10), 4053−4074.
(57) Shasteen, C.; Choy, Y. B. Controlling Degradation Rate of Poly(lactic Acid) for Its Biomedical Applications. *Biomed. Eng. Lett.* **2011**, *1* (3), 163.

https://dx.doi.org/10.1021/acsabm.0c00228
ACS Appl. Bio Mater. 2020, 3, 3236−3247